Stretchable EMI Measurement Sheet With 8 × 8 Coil Array, 2 V Organic CMOS Decoder, and 0.18 μm Silicon CMOS LSIs for Electric and Magnetic Field Detection

Koichi Ishida, *Member, IEEE*, Naoki Masunaga, Zhiwei Zhou, Tadashi Yasufuku, *Student Member, IEEE*, Tsuyoshi Sekitani, *Member, IEEE*, Ute Zschieschang, Hagen Klauk, Makoto Takamiya, *Member, IEEE*, Takao Someya, *Member, IEEE*, and Takayasu Sakurai, *Fellow, IEEE*

***Abstract*—A stretchable 12×12 cm^2 electromagnetic interference (EMI) measurement sheet is developed to enable the measurement of EMI distribution on the surface of electronic devices by wrapping the devices in the sheet. The sheet consists of an 8×8 coil array, a 2 V organic CMOS row decoder and a column selector, 40% stretchable interconnects with carbon nanotubes, and 0.18 μm silicon CMOS circuits for electric and magnetic field detection. The sheet detects the total power of an electric field in the band up to 700 MHz and that of a magnetic field up to 1 GHz. The minimum detectable powers of the electric and magnetic fields are −60 and −70 dBm, respectively.**

***Index Terms*—Calibration, carbon nanotubes, direct silicon-organic circuit interface, down conversion, electric filed, electromagnetic interference, frequency discrimination, intrasystem electromagnetic compatibility, localization, magnetic field, silicon CMOS, stretchable interconnects, stretchable measurement sheet, 2 V organic CMOS.**

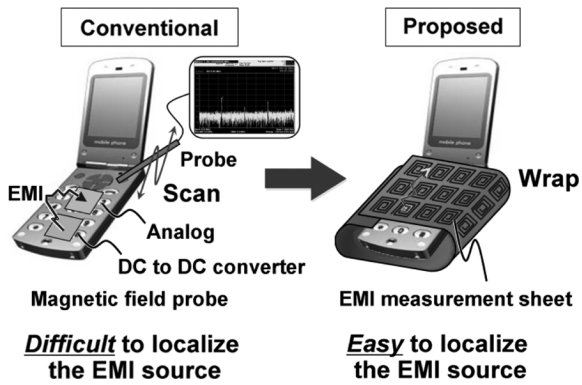

Fig. 1. An example of an intrasystem EMC issue in a mobile phone and the proposed EMI measurement.

I. Introduction

ELECTROMAGNETIC INTERFERENCE (EMI) that degrades the dependability of electronic devices is becoming a serious issue. The issue is complicated by the following technology trends: (1) RF signals and clock pulses of digital ICs are in the same frequency range. (2) The increase in LSI power consumption causes the increase in noise emission. (3) Electronic devices have 3-D structures and the packaging is dense. These trends also make it difficult to analyze the root cause of EMI. For example, it is difficult to find EMI generation points in electronic devices such as mobile phones and large flat-panel displays.

Fig. 1 shows an example of an intrasystem electromagnetic compatibility (EMC) issue in a mobile phone. EMI largely depends on the circuit board layout. Localizing either an EMI source or a critical wiring is difficult by simulation. EMI measurement is, therefore, important for the development of electronic devices. However, there is no method of measuring EMI on the surface of 3-D structures. In a conventional method, a pencil-like magnetic field probe with X-Y scanning equipment and spectrum analyzers are used for easy EMI measurement [1]. In the method, the surface of the electronic device should be scanned repeatedly with the probe. However, the scanning equipment can only move in a flat plane. In another conventional method, a measurement system with an integrated array of magnetic field loop antennas is used [2]. Although the method captures the distribution of a magnetic field, it is not applicable to 3-D structures since the antenna array is implemented in a piece of solid board.

To solve this problem, an EMI measurement sheet was proposed, which enables the measurement of EMI distribution on the surface of 3-D structures by wrapping the devices with a sheet like "*furoshiki*" [3]. Once EMI noise is roughly localized with the measurement sheet, one can easily scan EMI noise with

Manuscript received April 27, 2009; revised July 06, 2009. Current version published December 23, 2009. This paper was approved by Guest Editor Kevin Zhang. This work was supported in part by the Grant-in-Aid for Scientific Research, Special Coordination Funds for Promoting and Technology, NEDO, and CREST/JST.

K. Ishida, N. Masunaga, T. Yasufuku, and T. Sakurai are with the Institute of Industrial Science, University of Tokyo, Tokyo 153-8505, Japan (e-mail: ishida@iis.u-tokyo.ac.jp.)

Z. Zhou was with the Institute of Industrial Science, University of Tokyo, Tokyo 153-8505, Japan, and is now with Sony Corporation, Atsugi 243-0014, Japan.

T. Sekitani and T. Someya are with the Department of Electrical and Electronic Engineering, University of Tokyo, Tokyo 113-8654, Japan.

U. Zschieschang and H. Klauk are with the Max Planck Institute for Solid State Research, Stuttgart, Germany.

M. Takamiya is with the VLSI Design and Education Center, University of Tokyo, Tokyo 113-8654, Japan.

Digital Object Identifier 10.1109/JSSC.2009.2034446

the probe for precise localization. The magnetic field measurement using the sheet was demonstrated as shown in [3]. The sheet can measure not only a magnetic field but also an electric field by changing its antenna connection.

This paper describes the details of the EMI measurement sheet and the measurement result of both electric and magnetic fields. In Section II, we introduce the proposed EMI measurement sheet and the key technologies including 2 V organic CMOS and stretchable interconnects with carbon nanotubes (CNTs). In Section III, we describe the details of silicon CMOS LSIs for electric and magnetic field detection. In Section IV, we demonstrate the experimental results of both electric and magnetic fields with their frequency responses and provide some discussion. Finally, the conclusions are given in Section V.

II. Stretchable EMI Measurement Sheet

A. Stretchable EMI Measurement Sheet

To wrap 3-D structures such as mobile phones and large flat-panel displays, an EMI measurement sheet should be stretchable and flexible. The sheet includes a large number of arrayed antennas and measurement circuits, and therefore, large-area circuits such as a decoder and an encoder are required. We recognize that large-area electronic circuits should be implemented with organic CMOS to reduce cost and increase productivity. Recently, both the operation speed and supply voltage of organic transistors have been significantly improved [4]–[6]. In terms of operation speed, the inkjet technology in [6] realizes a 2 MHz cutoff frequency. However, this speed is not sufficient to handle EMI noise up to 1 GHz. We, therefore, recognize that the system-level integration of organic transistor and silicon CMOS circuit is essential for high-speed applications in large-area electronics. To realize a direct interface between organic transistors and silicon CMOS transistors, the sheet employs 2 V organic CMOS [4], [5] for the decoder and encoder, stretchable interconnects with CNTs [7], and the measurement circuit in a silicon CMOS LSI in this feasibility study.

Fig. 2 shows a prototype of the stretchable EMI measurement sheet. Each printed circuit board (PCB) includes 2×2 antenna coils and a silicon CMOS LSI chip. The sheet consists of 4×4 PCBs, and therefore, 8×8 antennas are located in 12×12 cm^2 area. The antennas and LSIs are controlled using a 2 V organic CMOS row decoder and a column selector. Each module is electrically connected with stretchable interconnects made of CNTs. The overall system is sealed with a rubber sheet made of silicone elastomer. The sheet is, therefore, flexible and stretchable.

Fig. 3 shows the block diagram of the EMI measurement sheet. Three-bit address and select signals are applied to the organic CMOS row decoder. The decoder selects one row of the arrayed EMI measurement circuit. Each select signal is connected to a PCB with rubber-like stretchable interconnects. Each PCB has a 2×2 antenna array to pick up EMI, an LSI, and six stretchable interconnects. The four antennas share the LSI to measure EMI. The outputs of silicon LSIs are connected to the organic CMOS column selector with stretchable interconnects. In the conventional integrated array of magnetic field antennas on a solid board [2], the processing function of the measured results is not integrated in the board. In contrast, the EMI measurement sheet has the LSIs distributed near the antennas for EMI measurement. It is the first demonstration of a distributed *in situ* EMI measurement, which has a potential to improve the measurement speed and accuracy. The diameter of the loop antenna is 9.8 mm. The antennas are made on a rigid PCB, because the antennas on a flexible film provide unstable antenna characteristics depending on the mechanical bending. When the scale of the array is large, a low-cost and large-area decoder is required to reduce the number of interconnects, and therefore, organic transistors are suitable for the decoder [8]. The performance of the sheet will improve as the operational speed of organic devices improves. In particular, a faster row decoder and column selector will realize high-speed scanning of the array.

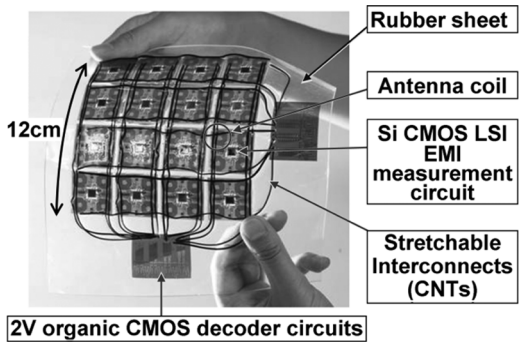

Fig. 2. Prototype of the stretchable EMI measurement sheet.

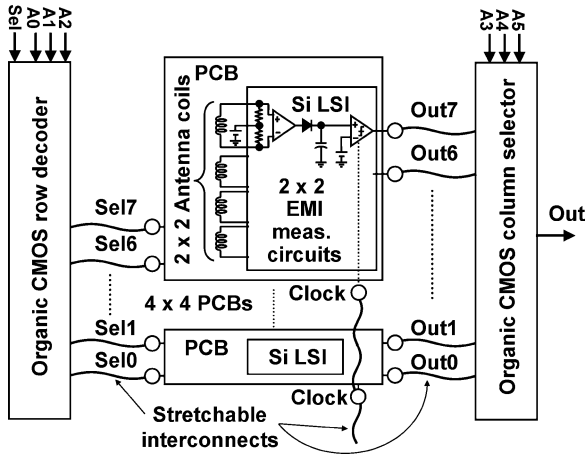

Fig. 3. Block diagram of the EMI measurement sheet.

B. 2 V Organic CMOS Decoder

In conventional organic design, only pMOS has been available and the power supply voltage was often as high as 40 V [8]. The low-gain circuits in the pMOS-only design and the high voltage make it difficult to interface organic circuits and LSI. To solve this problem, 2 V organic CMOS technology enabled by a 2.1-nm thick gate insulator (phosphoric acid self-assembled monolayers, SAM [4]) and the organic semiconductor (fluoroalkyl naphthalenetetracarboxylic di-imide, NTCDI [5]) for nMOS was developed. The device structure of the organic CMOS is shown in Fig. 4. An aluminum gate is deposited on the polyimide or silicon substrate by evaporation and the alumina is formed by oxygen plasma. SAM is overlaid by dip-coating.

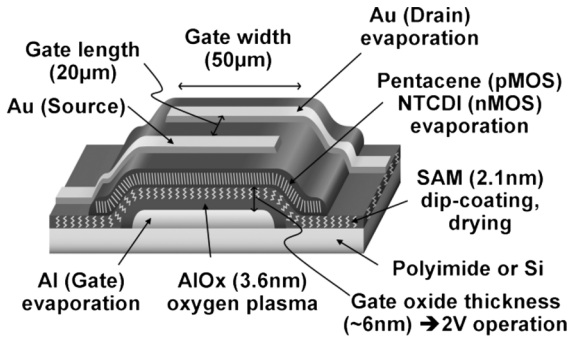

Fig. 4. Device structure of the 2 V organic CMOS transistor.

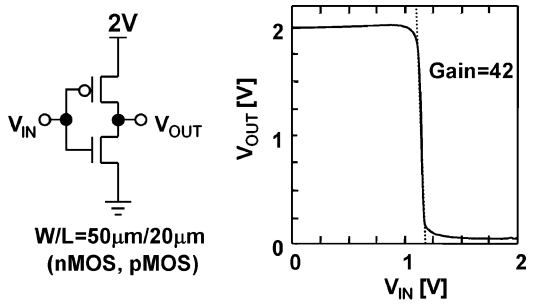

Fig. 5. (a) Schematic of the 2 V organic CMOS inverter. (b) Measured static characteristic of the inverter. Inverter gain of 42 is achieved with 2 V $\mathrm{V_{DD}}$.

Either pentacene for pMOS or NTCDI for nMOS is deposited on the gate oxide, and gold electrodes for drain and source are formed by evaporation. The sum of the alumina layer thickness of 3.6 nm and SAM layer thickness of 2.1 nm results in a total gate oxide thickness of 5.7 nm. Thanks to the technology of thin gate oxide, 2 V operation is realized. Organic/metallic hybrid passivation layers [9], not indicated in Fig. 4, protect organic CMOS and lengthen its lifetime to six months or more in air. On the other hand, [10] presents a long-life material for organic MOS transistors. The improvement of passivation layers and transistor materials will increase the lifetime of organic CMOS to years in the near future.

Fig. 5(a) shows a schematic of the organic CMOS inverter. The minimum gate length is determined using the metal mask resolution. Each gate width and length is 50 and 20 μm, respectively. Although organic nMOS transistors show poor driving capability compared with pMOS, both nMOS and pMOS are implemented with the same gate width because increasing the gate width degrades the transistor yield. Fig. 5(b) plots the measured static characteristic of the inverter. The inverter gain of 42, which is threefold the one shown in [12], is achieved with 2 V $\mathrm{V_{DD}}$. Since $\mathrm{V_{DD}}$ is decreased from 40 to 2 V, the organic CMOS can drive the silicon CMOS directly. Therefore, the first direct silicon-organic circuit interface is realized.

Fig. 6(a) shows the schematic of the 3 to 8 organic CMOS decoder. Three-bit address and select signals are applied and the decoder selects a row of LSI array to be operated. Since the organic CMOS technology allows direct signal transmission between organic circuits and LSIs, level shifters in [13] are eliminated. The column selector is similar to the row decoder. Instead of a common select signal, each of the Out0 to Out7 signals in

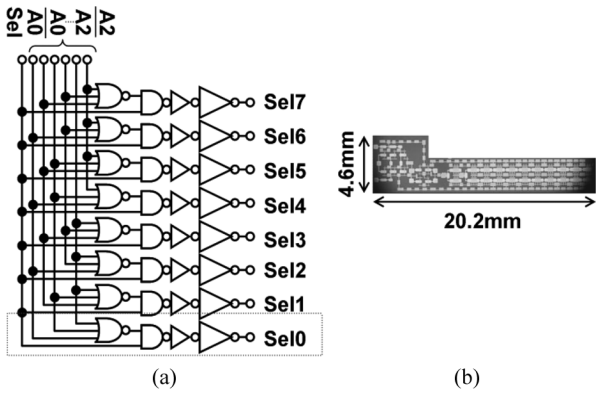

Fig. 6. (a) Schematic of the 3 to 8 organic CMOS decoder. (b) Photomicrograph of the decoder. The area of one bit is 4.6×20.2 mm^2.

Fig. 3 is applied individually to the different rows of NAND gates shown in Fig. 6(a). The output of each decoder is fed to an 8-input NAND to generate the global output signal.

Organic CMOS devices can be implemented on a polyimide or silicon substrate. In terms of performance and reliability, polyimide and silicon substrates achieve almost the same characteristics. A silicon substrate, however, provides both good handling for testing and the desired yield. Therefore, a key part of the organic decoder is fabricated on a silicon substrate in this work. However, the organic decoder should be implemented on a flexible substrate in a practical measurement sheet. The photomicrograph of the decoder is shown in Fig. 6(b). The area of one bit is 4.6×20.2 mm^2. Measurement results are shown in Section IV.

C. Stretchable Interconnects With CNTs

The conductive material for the stretchable interconnects is CNTs. CNTs are an inherently stretchable material with a very low resistivity of 0.02 $\mu\Omega$cm [7], however, CNTs should be disentangled prior to being combined with a rubberlike material. The process flow of the stretchable interconnects is shown in Fig. 7. Single-walled CNTs are used as a conductive material. An ionic liquid (1-butyl-3-methyl imidazoliumbis (trifluoromethanesulfonyl) imide, BMITFSI [7]) and CNTs are combined and ground to disentangle the CNTs. A rubberlike material, fluorinated copolymer, and CNT dispersed in gel are combined and stirred by sonication. The stretchable interconnects film is formed by air-drying. Fig. 8 demonstrates its stretchability. The flexible interconnects can be stretched by 40% thanks to the sliding CNTs embedded in the rubberlike material, fluorinated copolymer. The key features of the organic CMOS and stretchable interconnects are summarized in Table I.

III. Silicon CMOS LSI for EMI Detection

The typical frequency of concern with respect to EMI is from 30 MHz to 1 GHz as specified by the International Special Committee on Radio Interference (CISPR). If the measurement system tries to capture the waveform of EMI digitally as shown in Fig. 9(a), the sampling clock of the ADC should be higher than EMI noise by twofold or more. An advanced expensive silicon CMOS process is required to capture the waveform of EMI noise. Furthermore, the high-speed clock

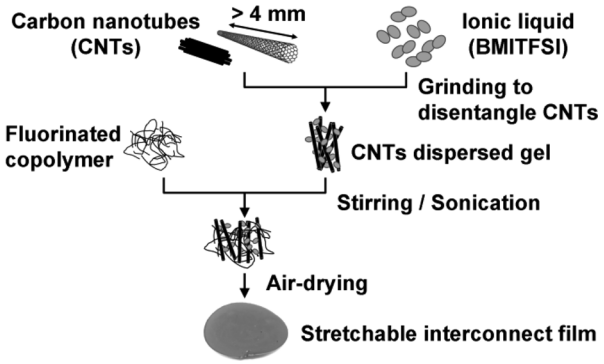

Fig. 7. Process flow of the stretchable interconnects with CNTs.

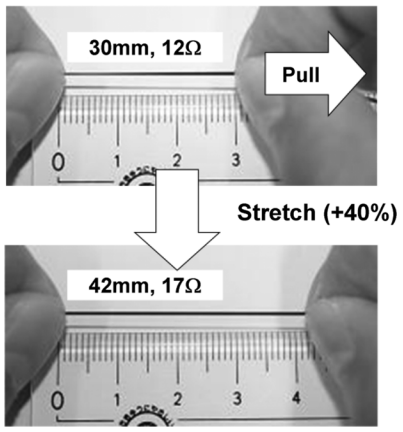

Fig. 8. Stretchability of the interconnects with CNTs. The resistant flexible interconnects can be stretched by 40%.

TABLE I
SUMMARY OF ORGANIC CMOS AND STRETCHABLE INTERCONNECTS

Organic CMOS material	Pentacene (pMOS) NTCDI (nMOS)
Supply voltage	2V
Inverter gain	42
Gate oxide thickness	6nm
Gate width / gate length	50μm / 20μm
Mobility	0.53 cm^2/Vs (pMOS) 0.03 cm^2/Vs (nMOS)
Stretchable interconnects material	Fluorinated copolymer, CNT
Stretchability	40%
Resistivity	0.02 Ωcm

pulses cause other noise problems such as clock distribution for an arrayed circuit and noise interference with the EMI noise to be measured. For the purpose of measuring the distribution of EMI power, however, it is not necessary to capture the noise waveform itself. The proposed circuit, therefore, employs a rectifier to convert the noise power to a DC voltage as shown

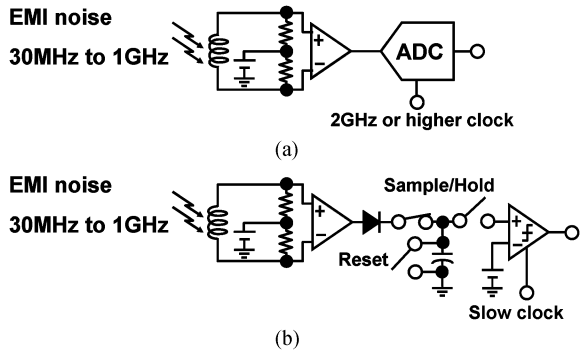

Fig. 9. Comparison of measurement methods. (a) Capturing the waveform of EMI digitally. (b) Converting EMI power to DC voltage using rectifier.

in Fig. 9(b). In this topology, a high-speed sampling clock that ranges from megahertz to gigahertz order is not required. Both the advanced expensive silicon CMOS process and clock interference issue can be avoided in this way.

Fig. 10 shows the circuit diagram and the timing chart of the proposed EMI measurement LSI. The LSI has a four-stage differential amplifier, an nMOS rectifier, sample and hold circuitry, and a comparator. The conventional integrated EMI sensor circuits [12] have analog outputs, which is unsuitable for array measurements because an analog signal is easily degraded during signal transportation. In contrast, the proposed EMI measurement LSI has a digital output, which is suitable for array measurements.

By changing the connection method of the antenna, the electric and magnetic fields are measured separately [14]. When both ends of the antenna are connected to the inputs of the differential amplifier, the magnetic field is measured, because the differential current in the antenna is amplified. On the other hand, when both ends of the antenna are connected to an input of the differential amplifier and the other input of the amplifier is connected to the bias voltage, the electric field is measured, because the common-mode current in the antenna is amplified.

For the aforementioned reason, the circuitry converts EMI noise waveform into DC voltage using the rectifier and the sample and hold circuits. The down conversion relaxes the requirement for the speed of the comparator, and the comparator can operate at low frequency such as 100 kHz. Fig. 11 shows the operation of the EMI measurement LSI. By adjusting the reference voltage (V_{REF}) of the comparator and the offset voltage of the rectifier, the comparator output shows 50% high-pulse density without EMI noise. The V_{TH} drop of the nMOS rectifier is canceled by AC coupling and adjusting DC bias on V_1 as shown in Fig. 10. Therefore, the rectified voltage correspondingly increases by increasing EMI noise. When the EMI power is large, the sampled voltage (V_3) is higher than the V_{REF}. The output of the comparator (V_{OUT}) is high. In contrast, when the EMI power is small, V_3 is lower than V_{REF}, and therefore, V_{OUT} is low. The V_{OUT} is reset to high at every clock (CompClk) edge, because the comparator is a clocked comparator. When the EMI power is medium, V_3 is close to V_{REF} and therefore, V_{OUT} changes between high and low. By sweeping V_{REF} and monitoring the pulse density of V_{OUT}, the

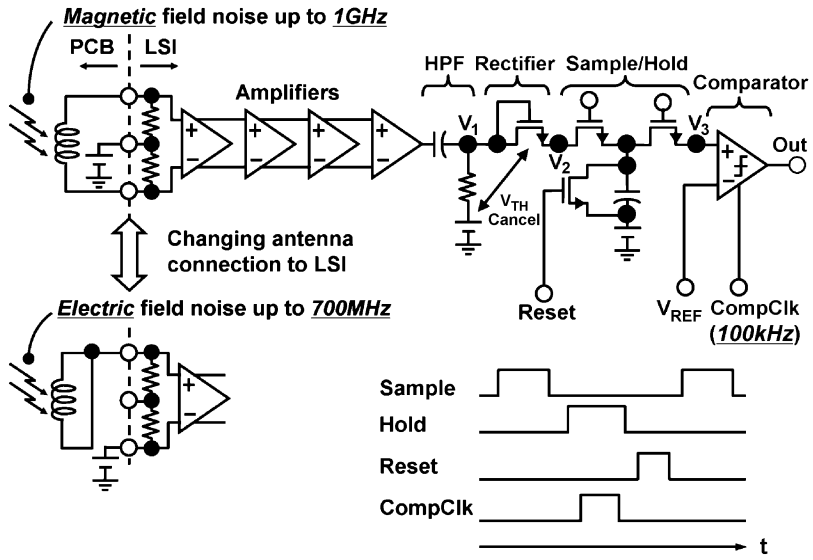

Fig. 10. Circuit diagram and timing chart of the proposed EMI measurement LSI.

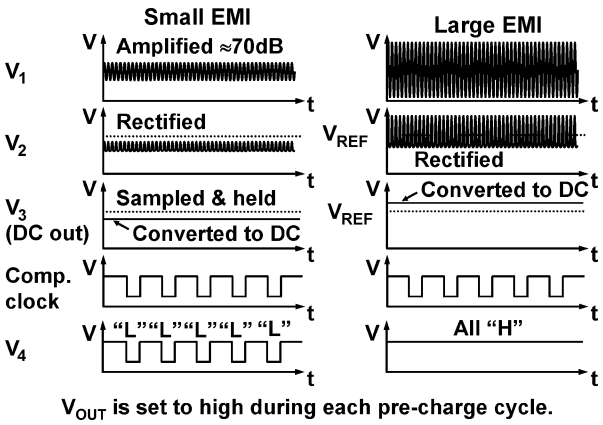

Fig. 11. Operation of the EMI measurement LSI.

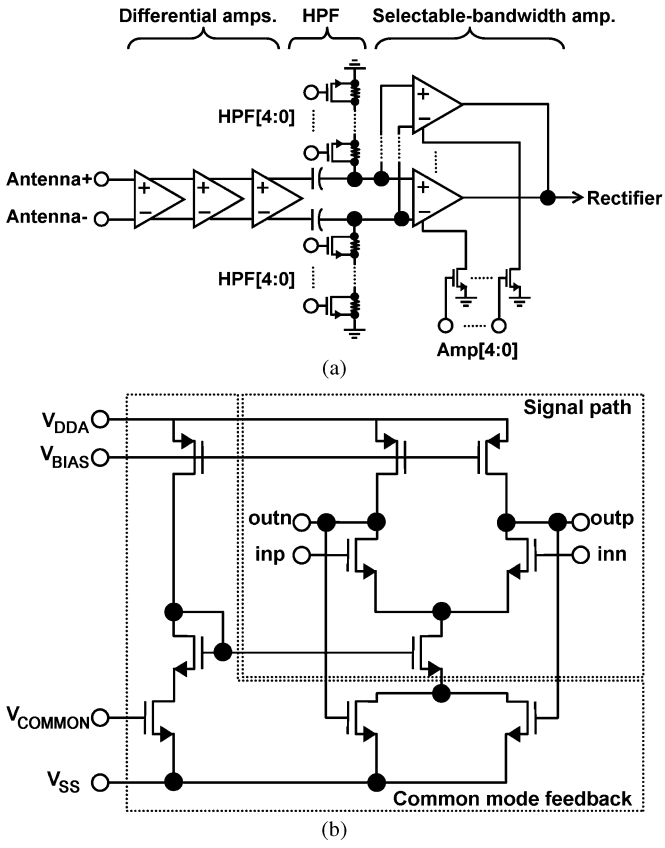

Fig. 12. (a) Detail of the four-stage differential amplifiers. (b) Schematic of each amplifier stage.

EMI power can be estimated. In this way, the EMI noise power is observed as a function of V_{REF}.

Fig. 12(a) and (b) shows the detail of the four-stage differential amplifier with a selectable bandwidth amplifier and the schematic of each amplifier stage, respectively. Common-mode voltage (V_{CM}) is determined by considering the threshold voltage of the nMOS rectifier. The total gain is approximately 80 dB, which enables the measurement of the magnetic EMI noise of -70 dBm, equivalent to 45 μV with a 50 Ω input resistance. Fig. 13 shows the simulated frequency response of the amplifiers. To avoid the noise interference caused by the 100 kHz sampling clock and its harmonics, a first-order high-pass filter (HPF) is adopted before the final stage amplifier. The bandwidth of the HPF can be changed by a five-bit digital code as shown in Figs. 12 and 13. To roughly estimate the EMI noise frequency, the bandwidth of the final-stage amplifier can also be changed by simply cutting off parallel transistors. Fig. 14 shows the die photomicrograph and layout of the EMI measurement LSI. The LSI is implemented in 1.8 V, 0.18 μm CMOS process, and the core area is 0.18 mm^2.

IV. Experimental Results and Discussion

A. Direct Silicon-Organic Circuit Interface

Fig. 15(a) shows the measurement setup for the direct signal transmission between the organic circuits, a part of the decoder in Fig. 6, and the LSI. The power supply voltage for both the organic circuits and LSI is 2.0 V. The organic circuits and LSI

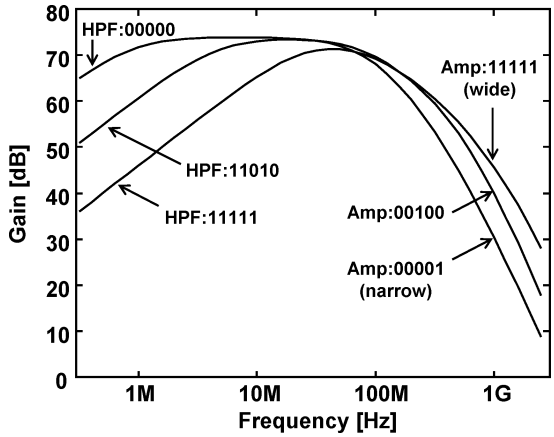

Fig. 13. Simulated frequency response of the four-stage amplifiers.

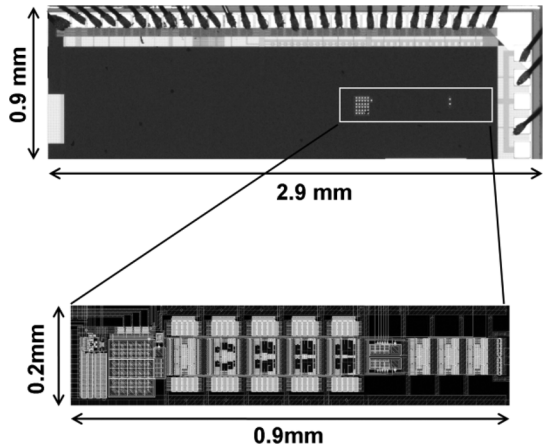

Fig. 14. Die photomicrograph and layout of the EMI measurement LSI.

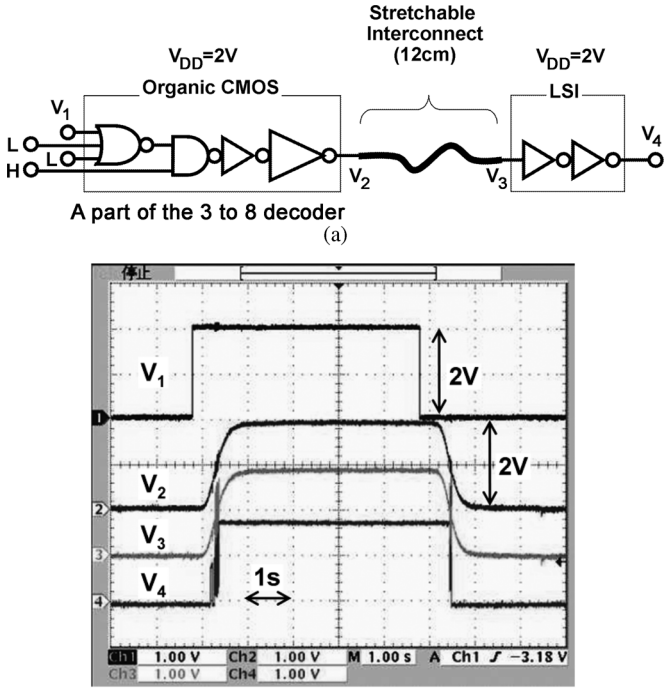

Fig. 15. (a) Measurement setup for the direct signal transmission between the organic circuits and an LSI. (b) Measured waveform of the direct silicon-organic interface.

are connected by a 12 cm stretchable interconnect. Its width is 1 mm, the thickness is 500 μm, the resistance is 48 Ω, and the resistivity is 0.02 Ωcm. Fig. 15(b) shows the measured waveform. V_1 and V_2 are input and output waveforms of the 2 V organic CMOS, respectively. V_3 is the output of the stretchable interconnect, that is, the input of silicon CMOS LSI. V_4 is the output of the LSI. As shown in Fig. 15(b), the organic CMOS decoder successfully drives the LSI without a level sifter. Both the rise and fall times of the output of the organic decoder are approximately 0.5 s, which is very slow but acceptable in this application. Although organic nMOS transistors show poor driving capability compared with pMOS, both nMOS and pMOS are implemented with the same gate length and width by considering the layout and yield. During the transmission of the input signal V_1 through several logic gates, both the rise and fall times of V_2, the output of the organic decoder, are limited by the driving capability of nMOS transistors rather than by the pMOS transistors or by the output load capacitance.

B. Comparison of Conventional and Proposed EMI Measurements

To demonstrate the operation of the EMI measurement sheet, the same magnetic EMIs measured with the conventional magnetic probe [1] and the developed EMI measurement sheet are compared. The DUT is a memory module in a laptop PC. Fig. 16(a) and (b) shows the photograph of the measurement setup and the spectrum of the measured magnetic EMI noise with the magnetic probe, respectively. The highest peak is -50 dBm at 267 MHz.

On the other hand, Fig. 17(a) shows the photograph of the measurement setup with the EMI measurement sheet. Fig. 17(b) and (c) shows the output waveforms of the developed EMI measurement LSI with and without DUT, respectively. In Fig. 17(b), the output shows a high pulse density of 81%, which detects EMI noise above the DUT. By contrast, in Fig. 17(c), the output includes no high pulse as described in Fig. 11, which detects no EMI noise without the DUT. Thus, the proposed system successfully detects the actual noise emitted by the memory module in the laptop PC.

C. Noise Frequency Estimation

Fig. 18(a) and (b) shows that the proposed LSI can roughly estimate EMI noise frequency by changing the bandwidth of the amplifier as shown in Fig. 13. EMI noise of 900 MHz is measured. Fig. 18(a) shows that the density of a high-pulse output from the comparator is 71% with a wide bandwidth setting, 45.8 dB total gain at 1 GHz. In contrast, Fig. 18(b) shows a density of 24% of a high-pulse output with a narrow bandwidth setting, 30.4 dB total gain at 1 GHz. This result indicates that the measured EMI noise frequency is high. If the measured EMI noise frequency is low such as 100 MHz, the difference in the high-pulse probability is negligible when changing the bandwidth of the amplifier. In this feasibility study, only the bandwidth of the final-stage amplifier can be selectable for easy estimation. Neither high-Q, high-order filters nor mixers are implemented. Therefore, the frequency discrimination of the

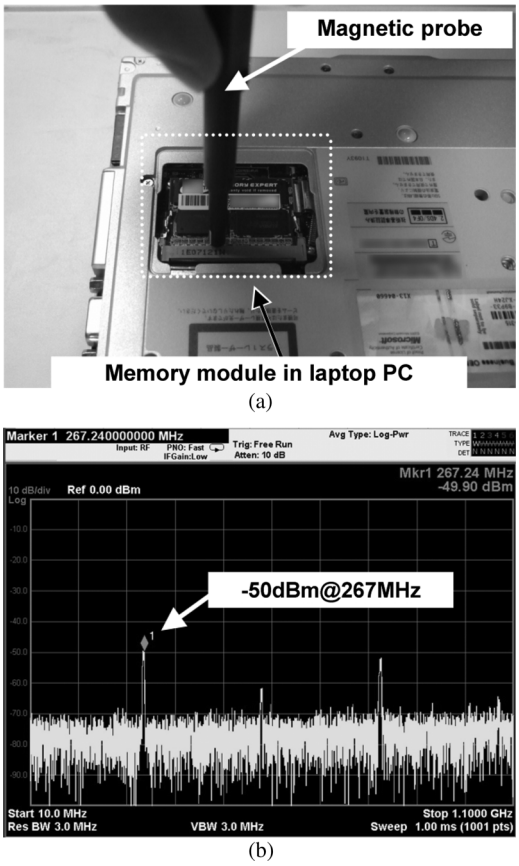

Fig. 16. Measured magnetic EMI noise with the conventional magnetic probe. (a) Measurement setup. (b) Spectrum of the noise.

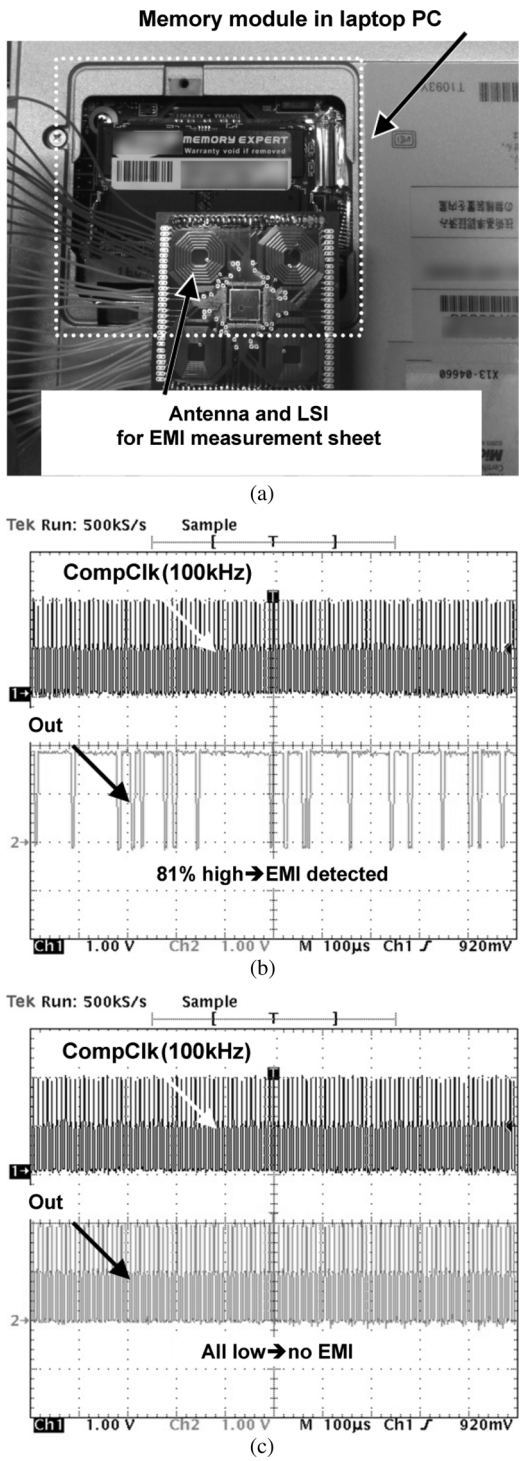

Fig. 17. Measured magnetic EMI noise with the EMI measurement sheet. (a) Measurement setup. (b) Output waveform with DUT. (c) Output waveform without DUT.

measurement sheet is not sufficient. To improve the frequency discrimination, high-Q, high-order filters and mixers should be added to the silicon CMOS circuit. By increasing the number of amplifiers of which the bandwidth can be selectable, EMI noise frequency can be also estimated more accurately.

D. Calibration for EMI Measurement LSI

To determine the absolute power of EMI and compensate the total gain of antenna coils and amplifiers, a calibration for the EMI measurement LSI is carried out. Fig. 19 shows the measurement setup to calibrate the frequency characteristics of the measurement of the electric and magnetic fields by the EMI measurement LSI. EMI noise is emulated using a signal generator and an antenna. The signal generator sweeps a sinusoidal wave up to 1 GHz. EMI noise is measured by the EMI measurement LSI and the commercial magnetic [1] and electric [15] field probes. The magnetic field probe detects power ranging from 10 MHz to 3 GHz within ± 1 dBμA/m error. The emulated EMI noise is monitored with the probe and the spectrum analyzer to calibrate the noise power. Similar to the magnetic field calibration, the electric field strength is calibrated using the electric field probe that can handle an electric field from 2 MHz to 2 GHz.

Fig. 20(a) shows the measured relationship between the magnetic field power and V_{REF} of the comparator when the comparator output shows 50% pulse density at different EMI frequencies in the EMI measurement LSI. V_{REF} correspondingly increases by increasing the magnetic field power. The result indicates that the input power of EMI is successfully converted into DC voltage by the nMOS rectifier and sample and hold circuit. The minimum detectable magnetic field noise power is -70 dBm. Once this calibration is carried out and the calibration table is established, the measurement sheet does not require further calibration. Fig. 20(b) shows the measured frequency response of the magnetic field power at different values of V_{REF}.

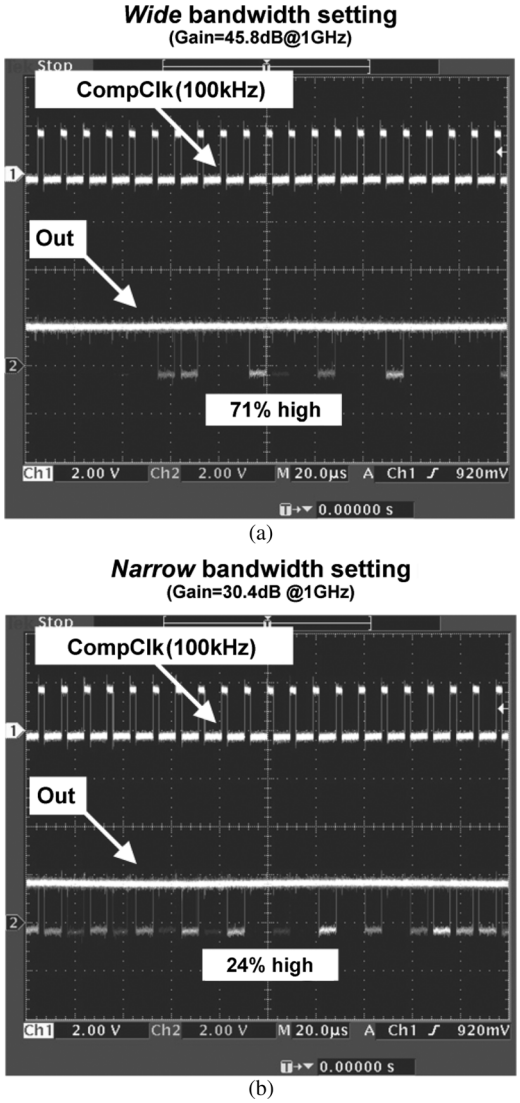

Fig. 18. Measured 900 MHz EMI noise with different bandwidths of the amplifiers. (a) Waveform with wide bandwidth setting. (b) Waveform with narrow bandwidth setting.

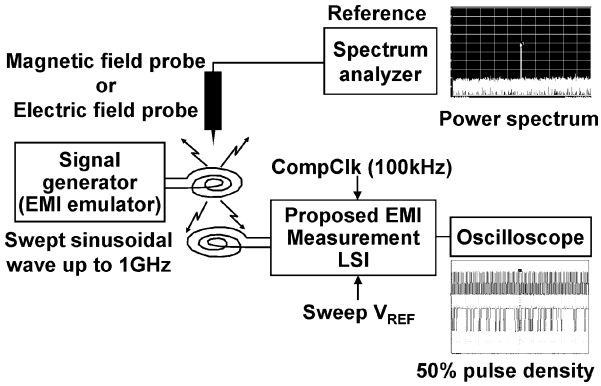

Fig. 19. Measurement setup for the calibration of the frequency response of the EMI measurement sheet.

The maximum detectable noise frequency achieves 1 GHz. An ideal frequency response should be flat. The measured magnetic result, however, shows that its sensitivity is degraded with increasing frequency. The frequency characteristic of the inductor of the spiral antenna coil is not flat and the frequency response of the amplifier gain shows bandpass characteristic as shown in Fig. 13. The measurement result reflects the frequency response of both antennas and amplifiers in the EMI measurement LSI.

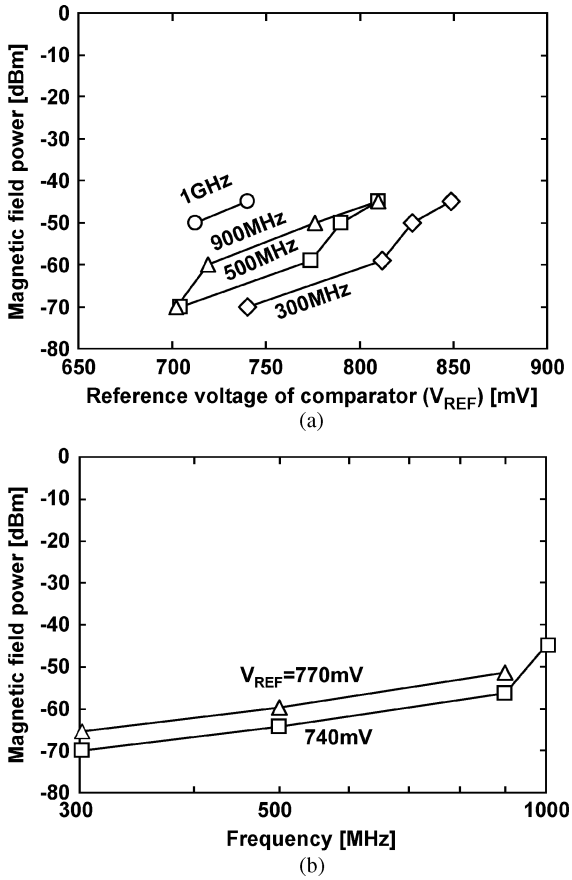

Fig. 20. Measured magnetic field power with the EMI measurement LSI. $\mathrm{V_{REF}}$ is a reference voltage of the comparator when the comparator output shows 50% pulse density. (a) $\mathrm{V_{REF}}$ dependence at different EMI frequencies. (b) Frequency response at different values of $\mathrm{V_{REF}}$.

Similar to the calibration of the magnetic field, Fig. 21(a) shows the measured relationship between the electric field power and $\mathrm{V_{REF}}$ at different EMI frequencies, and Fig. 21(b) shows the measured frequency response of the electric field power at different values of $\mathrm{V_{REF}}$. The minimum detectable electric field noise power is -60 dBm and the maximum detectable noise frequency is 700 MHz.

Comparison of the electric and magnetic field measurements shown in Figs. 20(a) and 21(a) reveals that the sensitivity of the electric field measurement is worse than that of the magnetic field measurement. The difference is attributable to the antenna gain difference between the electric and magnetic fields. The key features of the EMI measurement LSI are summarized in Table II.

In this feasibility study, the resolution of EMI localization and the flexibility of the measurement sheet are not sufficient to wrap mobile phones up because 9.8-mm-diameter antenna coils are employed. By using smaller antenna coils, both resolution and flexibility will be improved. In such a case, the gain

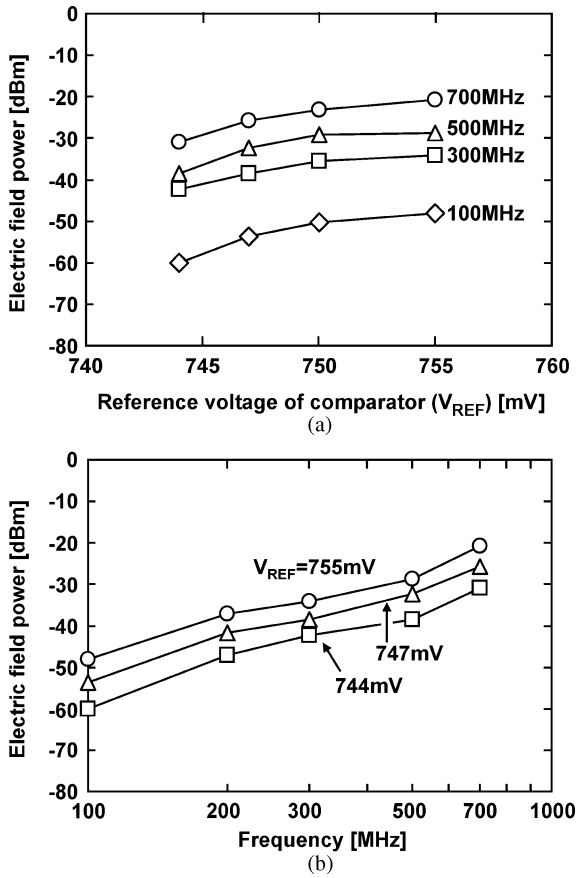

Fig. 21. Measured electric field power with the EMI measurement LSI. (a) $\mathrm{V_{REF}}$ dependence at different EMI frequencies. (b) Frequency characteristics at different values of $\mathrm{V_{REF}}$.

TABLE II
PERFORMANCE SUMMARY OF THE EMI MEASUREMENT LSI

Technology	1.8V, 0.18μm CMOS	
Core area	0.18mm^2	
Sampling frequency	100kHz	
Power consumption	110mW	
EMI Measurement	Magnetic field	Electric field
Minimum detectable noise power	-70dBm	-60dBm
Maximum detectable noise frequency	1GHz	700MHz

of amplifiers should be enhanced to compensate for the smaller antenna gain. To enhance the minimum detectable power of both magnetic and electric field measurements, the total gain of antenna coil and amplifiers should be improved particularly in the high frequency region. In terms of self-resonant frequency, smaller antennas generally provide better inductive characteristics. However, the capacitive characteristics are degraded with smaller antennas, and therefore, further amplifier gain will be required. This may not be a reasonable solution. In terms of resolution, minimum detectable power, and frequency discrimination, a down conversion scheme with a mixer is required to enhance the performance of the EMI measurement LSI.

V. CONCLUSION

The direct silicon-organic circuit interface has been demonstrated for the first time. The system-level integration of silicon CMOS technology, 2 V organic CMOS technology, and stretchable interconnects including carbon nanotubes makes a stretchable EMI measurement sheet possible, and the proposed LSI demonstrates EMI noise measurement up to 1 GHz using a rectifier and comparator operating at only 100 kHz. By changing the connection of the antenna to the LSI, the electric and magnetic fields are successfully measured separately. The minimum detectable magnetic field noise power is -70 dBm and the maximum detectable noise frequency is 1 GHz. The minimum detectable electric field noise power is -60 dBm and the maximum detectable noise frequency is 700 MHz.

ACKNOWLEDGMENT

The authors would like to thank S. Kazama, H. Tsutagaya, and M. Sakurada from Taiyo Yuden Co., Ltd. for fruitful discussions.

REFERENCES

[1] Magnetic Field Probe (CP-2S), NEC Corp., Japan.
[2] EMSCAN. [Online]. Available: http://www.emscan.com/
[3] K. Ishida, N. Masunaga, Z. Zhou, T. Yasufuku, T. Sekitani, U. Zschieschang, H. Klauk, M. Takamiya, T. Someya, and T. Sakurai, "A stretchable EMI measurement sheet with 8 × 8 coil array, 2 V organic CMOS decoder, and −70 dbm EMI detection circuits in 0.18 μm CMOS," in *IEEE Int. Solid-State Circuits Conf. (ISSCC) Dig. Tech. Papers*, Feb. 2009, pp. 472–473.
[4] H. Klauk, U. Zschieschang, J. Pflaum, and M. Halik, "Ultralow-power organic complementary circuits," *Nature*, vol. 445, pp. 745–748, Feb. 2007.
[5] H. E. Katz, A. J. Lovinger, J. Johnson, C. Kloc, T. Siegrist, W. Li, Y.-Y. Lin, and A. Dodabalapur, "A soluble and air-stable organic semiconductor with high electron mobility," *Nature*, vol. 404, pp. 478–481, Mar. 2000.
[6] T. Sekitani, Y. Noguchi, U. Zschieschang, H. Klauk, and T. Someya, "Organic transistors manufactured using inkjet technology with subfemtoliter accuracy," in *Proc. National Academy of Sciences USA*, Apr. 2008, vol. 105, no. 13, pp. 4976–4980.
[7] T. Sekitani, Y. Noguchi, K. Hata, T. Fukushima, T. Aida, and T. Someya, "A rubberlike stretchable active matrix using elastic conductors," *Science*, vol. 321, pp. 1468–1472, Sep. 2008.
[8] H. Kawaguchi, T. Someya, T. Sekitani, and T. Sakurai, "Cut-and-paste customization of organic FET integrated circuit and its application to electronic artificial skin," *IEEE J. Solid-State Circuits*, vol. 40, no. 1, pp. 177–185, Jan. 2005.
[9] T. Sekitani and T. Someya, "Air-stable operation of organic field-effect transistors on plastic films using organic/metallic hybrid passivation layers," *Jpn. J. Appl. Phys.*, vol. 46, no. 7A, pp. 4300–4306, Jul. 2007.
[10] T. Yamamoto and K. Takimiya, "Facile synthesis of highly pi-extended heteroarenes, dinaphtho[2,3-b:2′, 3′- f]chalcogenopheno [3,2-b]chalcogenophenes, and their application to field-effect transistors," *J. Amer. Chem. Soc.*, vol. 129, no. 8, pp. 2224–2225, 2007.
[11] S. De Vusser, S. Steudel, K. Myny, J. Genoe, and P. Heremans, "A 2 V organic complementary inverter," in *IEEE Int. Solid-State Circuits Conf. (ISSCC) Dig. Tech. Papers*, Feb. 2006, pp. 1082–1083.

[12] S. Aoyama, S. Kawahito, T. Yasui, and M. Yamaguchi, "A high-sensitivity active magnetic probe using CMOS integrated circuits technology," in *Proc. IEEE Topical Meeting on Electrical Performance of Electronic Packaging*, Oct. 2005, pp. 103–106.
[13] M. Takamiya, T. Sekitani, Y. Miyamoto, Y. Noguchi, H. Kawaguchi, T. Someya, and T. Sakurai, "Design solutions for multi-object wireless power transmission sheet based on plastic switches," in *IEEE Int. Solid-State Circuits Conf. (ISSCC) Dig. Tech. Papers*, Feb. 2007, pp. 362–363.
[14] S. Kazama and K. Arai, "Adjacent electric field and magnetic field distribution measurement system," in *Proc. IEEE Int. Symp. Electromagnetic Compatibility*, Aug. 2002, vol. 1, pp. 395–400.
[15] Electric Field Probe (CTM030), Credence Technologies [Online]. Available: http://www.credencetech.com/products/product.php?productId=CTK031

Koichi Ishida (S'00–M'06) received the B.S. degree in electronics engineering from the University of Electro-Communications, Tokyo, Japan, in 1998, and received the M.S. and Ph.D. degrees in electronics engineering from the University of Tokyo, Tokyo, Japan, in 2002 and 2005, respectively.

He joined Nippon Avionics Co., Ltd. Yokohama, Japan in 1989, where he developed high-reliability hybrid microcircuits applied to aerospace programs. Since July 2007, he has been working at Institute of Industrial Science, the University of Tokyo as a research associate. His research interests include low-voltage low-power CMOS analog circuits, RF wireless-communication circuits, and on-chip power supplies. He is a member of IEEE and IEICE.

Naoki Masunaga received the B.S. degree in electronic engineering from Sophia University, Tokyo, Japan, in 2008. He is currently studying in Graduate school of Engineering, The University of Tokyo. His research interests are in the field of integrated circuit design.

Zhiwei Zhou received the M.S. degree in electronic engineering from University of Tokyo, Japan, in 2008. His research interests include the circuit design of the low-power RF receiver circuits. He is now with Sony Corporation.

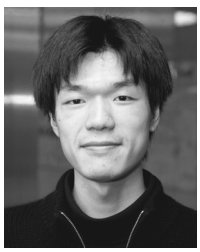

Tadashi Yasufuku (S'09) received the B.S. degree in applied physics from Keio University, Japan in 2007, and the M.S. degree in electronic engineering from the University of Tokyo, Japan, in 2009. He is currently working toward the Ph.D, degree. His research interests include sub/near threshold logic circuit design and switched converters.

Tsuyoshi Sekitani was born in Yamaguchi, Japan, in 1977. He received the B.S. degree from Osaka University, Japan, and the Ph.D. degree in applied physics from the University of Tokyo, Japan, in 1999 and 2003, respectively.

From 1999 to 2003, he was with the Institute for Solid State Physics (ISSP), University of Tokyo. From 2003 to 2009, he was a Research Associate of the Quantum-Phase Electronics Center, University of Tokyo. Since 2009, he has been a Research Associate of Department of Electrical and Electronic Engineering, University of Tokyo.

Ute Zschieschang received the Dipl.-Ing. FH, Oberflächentechnik, Fachhochschule Mittweida in 2000, and the Dr. rer. nat., Chemie, Technische Universität Bergakademie Freiberg in 2006. In 2005, she joined the Max Planck Institute for Solid State Research in Stuttgart, Germany.

Hagen Klauk received the Diplom-Ingenieur degree in Electrical Engineering from Chemnitz University of Technology (Germany) in 1995, and the Ph.D. degree in electrical engineering from the Pennsylvania State University in 1999.

From 2000 to 2005 he was with the Polymer Electronics group at Infineon Technologies in Erlangen, Germany. In 2005 he joined the Max Planck Institute for Solid State Research in Stuttgart, Germany, to lead an Independent Junior Research Group in organic electronics.

Makoto Takamiya (S'98–M'00) received the B.S., M.S., and Ph.D. degrees in electronic engineering from the University of Tokyo, Japan, in 1995, 1997, and 2000, respectively.

In 2000, he joined NEC Corporation, Japan, where he was engaged in the circuit design of high speed digital LSIs. In 2005, he joined University of Tokyo, Japan, where he is an associate professor of VLSI Design and Education Center. His research interests include the circuit design of the low-power RF circuits, the ultra low-voltage digital circuits, and the large area electronics with organic transistors.

Dr. Takamiya is a member of the technical program committee for IEEE Symposium on VLSI Circuits and IEEE Custom Integrated Circuits Conference (CICC).

Takao Someya (M'03) received the Ph.D. degree in electrical engineering from the University of Tokyo, Japan, in 1997.

In 1997, he joined Institute of Industrial Science (IIS), the University of Tokyo, as a Research Associate and was appointed to be a Lecturer of the Research Center for Advanced Science and Technology (RCAST), University of Tokyo, in 1998, and an Associate Professor of RCAST in 2002. From 2001 to 2003, he worked for the Nanocenter (NSEC) of Columbia University and Bell Labs, Lucent Technologies, as a Visiting Scholar. From 2003 to 2009, he was an Associate Professor of the Department of Applied Physics and Quantum-Phase Electronics Center, the University of Tokyo. Since 2009, he has been a Professor of electrical and electronic engineering at the University of Tokyo. His current research interests include organic transistors, flexible electronics, plastic integrated circuits, large-area sensors, and plastic actuators.

Prof. Someya is a member of the IEEE Electron Devices Society, the Materials Research Society (MRS), and the Japanese Society of Applied Physics. He serves as a subcommittee member for IEEE/IEDM and a program co-chair for the 3rd Organic Microelectronics Workshop.

Takayasu Sakurai (S'77–M'78–SM'01–F'03) received the Ph.D. degree in electrical engineering from the University of Tokyo, Japan, in 1981.

In 1981 he joined Toshiba Corporation, where he designed CMOS DRAM, SRAM, RISC processors, DSPs, and SoC Solutions. He has worked extensively on interconnect delay and capacitance modeling known as Sakurai model and alpha power-law MOS model. From 1988 through 1990, he was a visiting researcher at the University of California Berkeley, where he conducted research in the field of VLSI CAD. From 1996, he has been a professor at the University of Tokyo, working on low-power high-speed VLSI, memory design, interconnects, ubiquitous electronics, organic ICs and large-area electronics. He has published more than 400 technical publications including 100 invited presentations and several books and filed more than 200 patents.

Dr. Sakurai will be an executive committee chair for VLSI Symposia and a steering committee chair for IEEE A-SSCC from 2010. He served as a conference chair for the Symp. on VLSI Circuits, and ICICDT, a vice chair for ASPDAC, a TPC chair for the A-SSCC, and VLSI symp., an execcuitve committee member for ISLPED and a program committee member for ISSCC, CICC, A-SSCC, DAC, ESSCIRC, ICCAD, ISLPED, and other international conferences. He is a recipient of 2010 IEEE Donald O. Pederson Award in Solid-State Circuits, 2009 achievement award of IEICE, 2005 IEEE ICICDT award, 2004 IEEE Takuo Sugano award and 2005 P&I patent of the year award and four product awards. He gave keynote speech at more than 50 conferences including ISSCC, ESSCIRC and ISLPED. He was an elected AdCom member for the IEEE Solid-State Circuits Society and an IEEE CAS and SSCS distinguished lecturer. He is a STARC Fellow, IEICE Fellow and IEEE Fellow.